

# Aluminum Metasurface with Hybrid Multipolar Plasmons for 1000-Fold Broadband Visible Fluorescence Enhancement and Multiplexed Biosensing

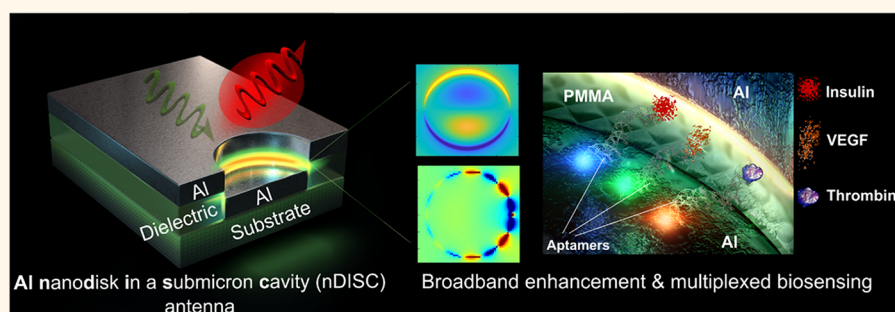
Radwanul Hasan Siddique,<sup>†,§,||</sup> Shailabh Kumar,<sup>†,||</sup> Vinayak Narasimhan,<sup>†</sup> Hyounghan Kwon,<sup>†</sup> and Hyuck Choo<sup>\*,†,‡,§</sup>

<sup>†</sup>Department of Medical Engineering, California Institute of Technology, 1200 E. California Boulevard, MC 136-93, Pasadena, California 91125, United States

<sup>‡</sup>Department of Electrical Engineering, California Institute of Technology, 1200 E. California Boulevard, MC 136-93, Pasadena, California 91125, United States

<sup>§</sup>Samsung Advanced Institute of Technologies, Samsung Electronics, 130 Samseong-ro, Maetan-dong, Yeongtong-gu, Suwon, Gyeonggi-do 16678, South Korea

## Supporting Information



**ABSTRACT:** Aluminum (Al)-based nanoantennae traditionally suffer from weak plasmonic performance in the visible range, necessitating the application of more expensive noble metal substrates for rapidly expanding biosensing opportunities. We introduce a metasurface comprising Al nanoantennae of nanodisks-in-cavities that generate hybrid multipolar lossless plasmonic modes to strongly enhance local electromagnetic fields and increase the coupled emitter's local density of states throughout the visible regime. This results in highly efficient electromagnetic field confinement in visible wavelengths by these nanoantennae, favoring real-world plasmonic applications of Al over other noble metals. Additionally, we demonstrate spontaneous localization and concentration of target molecules at metasurface hotspots, leading to further improved on-chip detection sensitivity and a broadband fluorescence-enhancement factor above 1000 for visible wavelengths with respect to glass chips commonly used in bioassays. Using the metasurface and a multiplexing technique involving three visible wavelengths, we successfully detected three biomarkers, insulin, vascular endothelial growth factor, and thrombin relevant to diabetes, ocular and cardiovascular diseases, respectively, in a single 10  $\mu\text{L}$  droplet containing only 1 fmol of each biomarker.

**KEYWORDS:** *nanoplasmonics, scalable metasurface, aluminum plasmonics, strong light–matter interaction, fluorescence enhancement, multiplexed biosensing*

Near-field enhancement of optical signals from biomolecules *via* optical nanoantennae has played a significant role in breakthroughs in areas such as single molecule fluorescence-driven DNA sequencing,<sup>1,2</sup> sensitive biosensing for early disease detection,<sup>3–5</sup> and analyzing biochemical interactions.<sup>6</sup> While noble metals like gold (Au) and silver (Ag) have been the dominant materials of choice for these applications,<sup>3–8</sup> search for alternatives that are cost-

effective and robust has led to detailed exploration of other materials such as aluminum (Al) and titanium nitride<sup>9–13</sup> in recent years. Al especially has the potential to become an

**Received:** April 15, 2019

**Accepted:** November 5, 2019

**Published:** November 5, 2019

excellent alternative due to its abundance, sustainability, and simple processing requirements.<sup>10,12,14</sup> Most importantly, Al leads over other noble metals in terms of plasma frequency that lies at a higher energy. Despite their promise, Al nanoantennae have mostly been limited to biosensing applications in the ultraviolet (UV) to blue wavelength regimes due to the inherently low quality factors ( $Q$ ) of dipolar surface plasmons resonances ( $Q: \sim 2$ ) in the visible range as compared to Ag ( $Q: 5-10$ ) and Au ( $Q: 10-20$  in red).<sup>15-17</sup> One way to overcome this issue could be utilizing higher order plasmonic modes of large aluminum nanoantennae with lower radiative and interband damping over the optical spectra.<sup>15,18</sup> However, higher order plasmons are dark (subradiant) in nature with almost zero net-dipole moment, that is, they do not easily couple with incident photons, and therefore they are not preferred in optical applications.<sup>19</sup> Very recently, it has been shown that the plasmonic dark modes can be bright (super-radiant) and radiative in the far-field of tightly spaced nanostructures caused by symmetry breaking, allowing us to observe strong light-matter coupling at a single molecule level.<sup>20-23</sup>

By employing this principle with the aforementioned property of Al, we show that the higher-order hybrid plasmon resonance modes of the submicron Al nanoantennae can enhance the local optical fields and fluorescence emission significantly, resulting in 1000-fold enhancement in the visible range. Our metasurface is comprised of a nanoantenna array composed of Al nanodisks in submicron cavities (nDISC) that serve as out-of-plane metal-insulator-metal (MIM) nanoantenna and allows extremely efficient light transfer between the far- and near-fields in the visible spectrum (Figure 1). To maximize the use of this efficient light transfer, we changed the insulator material from oxide ( $\text{SiO}_2$ ) to polymer (poly(methyl methacrylate) (PMMA)),

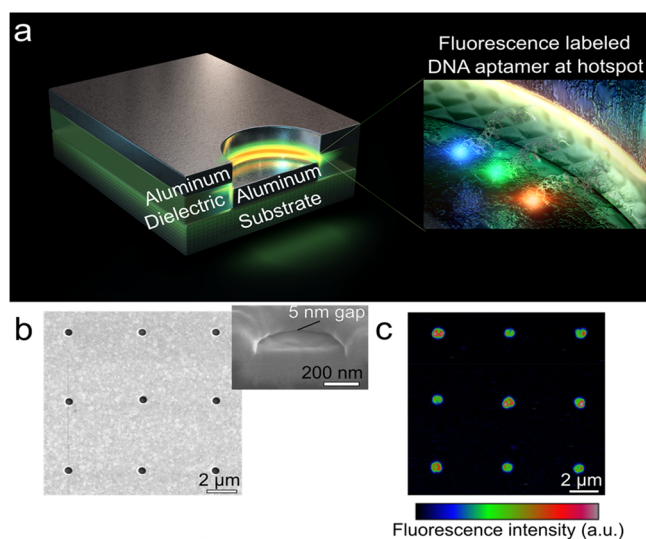


**Figure 1.** Aluminum nanodisk inside a submicron cavity (nDISC) nanoantenna for visible fluorescence enhancement. (a) Schematic of Al nDISC nanoantenna separated with 5 nm gap dielectric, which acts as an electromagnetic hotspot as well as biomolecule capturing site. (b) SEM image of an array of milled nDISC by milling holes on a silica film followed by Al deposition. High-resolution SEM inset confirms the 5 nm gap. (c) Confocal fluorescence image of the 9 nDISC nanoantenna coated with 1  $\mu\text{M}$  Cy3-labeled single-stranded DNA. The coffee-bean-shaped intensity profiles are result of direct fluorescent enhancement from the gap hotspot (excitation power  $-0.2$  mW, laser residence time 8.24  $\mu\text{s}/\text{pixel}$ , frame time  $-40.5$  s).

which allowed spatially preconcentrating local molecules at the electromagnetic hotspots spontaneously and further increased the fluorescence signal. In addition, we applied a biomimetic approach to create a highly scalable fabrication process suitable for industry relevant applications using only spin coating of a binary polymer blend solution and metal evaporation. Greatly benefiting from optical enhancement and molecular concentration, fabricated nDISC metasurfaces accomplished a high electromagnetic enhancement factor ( $>100$ ) and consequently fluorescence enhancement factor ( $f_E$ ) ( $>1000$ ) throughout the visible range compared to glass chips. The metasurfaces were then successfully utilized for substrate-enhanced, multiplexed, broadband detection of biomarkers in the visible range, including insulin, vascular endothelial growth factor (VEGF), and thrombin at a physiologically important, low concentration level (100 pM),<sup>24,25</sup> promising a simple, effective way to provide early detection of diseases as well as clinical needs.

## RESULTS AND DISCUSSION

The nDISC nanoantenna concept is illustrated in Figure 1a. Using focused ion beam (FIB), we milled a  $3 \times 3$  array of 500 nm diameter cavities in  $\text{SiO}_2$ , followed by Al evaporation to create a nanodisk inside each nanocavity (Figure 1b). The  $\sim 5$  nm  $\text{SiO}_2$  layer between the Al disk (metal) and cavity (metal, Al) provides optical field confinement that forms a hotspot (Figure 1b inset) and allows biomolecules to directly access the hotspots (Figure 1a). Figure 1c shows the doughnut-shaped intensity profiles from a confocal fluorescence scan of 1  $\mu\text{M}$  30-basepair-long single-stranded DNA linked with visible Cy3 fluorophore (excitation: 555 nm, emission: 568 nm with an intrinsic quantum yield,  $\eta_0 = 0.11$ ), confirming the significant signal enhancement of the molecule diffusing around the hotspot. The experimentally measured fluorescence enhancement  $f_E$  is  $956 \pm 172$ , which is commensurate with the fluorescence enhancement levels of low quantum yield dye obtained using gold-based nanoantennae.<sup>6-8</sup> In order to calculate the enhancement factor, we compare the fluorescence obtained on nDISC samples with  $\text{SiO}_2$  nanorings with standard microscopy glass slides, which are commonly used in bioassays (see Supporting Information (SI) for more details.) We chose Cy3 as our test dye because of its low intrinsic quantum yield (10%) that supports higher enhancement from an optical antenna.<sup>7,8</sup> This is an extremely encouraging result for visible Al plasmonics because plasmons on aluminum surfaces are known to suffer from huge losses, especially in the visible domain.

This fluorescence enhancement *via* Al nDISC antenna occurs due to simultaneous boost of local electric field ( $E$ ) and local density of states (LDOS) on the emitting molecule's excitation and emission, respectively, due to substantial energy transfer from antenna plasmon modes at the hotspot. Therefore, the maximum theoretical  $f_E$  can be calculated by considering field-aligned dipole moments of the emitter:<sup>26</sup>

$$f_E = \left| \frac{E}{E_0} \right|^2 \times \frac{\eta}{\eta_0}$$

where  $E$  indicates the enhanced excitation field over incident electric field,  $E_0$  and  $\eta$  accounts for the modified quantum yield of the fluorescence emitter owing to an increase in LDOS. In order to understand the origin of such improvement on both excitation and emission, we performed finite-difference time-domain (FDTD) simulations using a Maxwellian equation

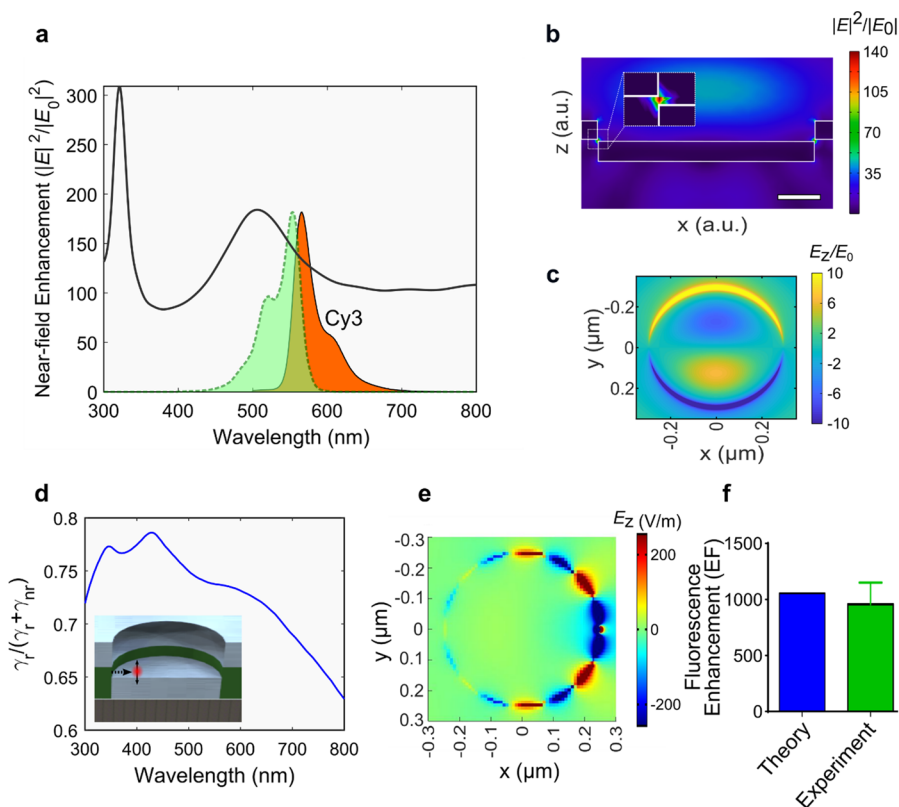


**Figure 2.** Simulation of strong visible fluorescence enhancement by nDISC nanoantenna. (a) Numerical simulations of the maximum near-field enhancement at the hotspot of 500 nm Al nDISC nanoantenna along with the excitation (dotted green line) and emission (solid orange line) of the test Cy3 dye. (b) The calculated normalized electric field intensity  $|E|^2/|E_0|^2$  at the Cy3 dye excitation peak wavelength ( $\lambda = 555$  nm) of Al nDISC shows a strong field confinement within the 5 nm gap between the disk and cavity. (c) The electric field profile at the horizontal plane in the middle of the hotspot (2.5 nm distance from the disk, cavity and insulator,  $\lambda = 555$  nm) corroborates the contribution of multipolar plasmon resonances on the field enhancement. (d) The FDTD simulations of a single emitting fluorescent molecule near an Al nDISC nanoantenna (dipole placed 2.5 nm to the side as shown in the inset) show broadband visible radiative enhancement ( $\gamma_r$ ) over the total radiative ( $\gamma_r$ ) and nonradiative ( $\gamma_{nr}$ ) enhancement. (e) Enhanced emission at 568 nm (emission peak of Cy3) shown at the horizontal plane in the middle of the hotspot (2.5 nm distance from the disk and cavity) occurs due to coupling to higher order plasmons modes at the hotspot. The intensity of the field is asymmetric due to better coupling of emitter emission to the closer available plasmonic modes with respect to the farthest ones. (f) Bar plot of theoretical and experimental fluorescence enhancements of 500 nm Al nDISC nanoantenna shows the 1000-fold fluorescence signal improvement in the visible domain ( $\lambda_{exc} = 555$  nm,  $\lambda_{em} = 568$  nm).

solver Lumerical. We calculated the near-field enhancement of fabricated nDISC antenna including a 3 nm-thick native alumina layer as shown in Figure 2a along with the excitation and emission fluorescence spectra of Cy3. The nDISC antenna shows significant near-field enhancement in the visible regime with strong  $Q$  of  $\sim 6$ . The experimentally obtained dark-field scattering profile of 500 nm nDISC nanoantenna also shows a similar pattern to near-field enhancement (Figure S1) with a slightly lower  $Q$  ( $\sim 4.2$ ) value probably due to the inherent surface roughness of the evaporated metal. The maximum excitation-intensity enhancement  $\left| \frac{E}{E_0} \right|^2$  is found to be 145 at the nDISC antenna hotspot as shown in Figure 2a,b using the excitation wavelength of Cy3 (555 nm), which is an improvement in performance over previously reported Al nanoantennas.<sup>27,28</sup> The  $E_z$  profile in Figure 2c which is the out-of-plane field component at the hotspot clearly reveals that the hybrid quadrupolar mode is responsible for such strong field intensity.

The scattering strength of the higher order resonances exhibited by individual (lone) Al nanodisk (Figure S2) is extremely poor due to high nonradiative damping and weak coupling to incident light.<sup>14,29</sup> Moreover, the dipolar plasmon

resonant wavelength and their respective resonance line width supported by a lone Al nanodisk rapidly increases as a function of its diameter due to higher radiative damping.<sup>12,14,29</sup> For example, we simulated the scattering profile of a 75–175 nm lone Al nanodisk to excite the dipolar resonances peaking at the visible regime (Figure S2) and found the average  $Q$  to be only 2 which is also in agreement with previous literatures.<sup>12,14,29</sup> In contrast, the simulated scattering and electric field profiles of 50–500 nm nDISC antenna shown in Figure S3 demonstrate that nDISC nanoantenna possess strong scattering peaks on account of plasmonic hybrid modes. The  $Q$  factors of the hybrid modes vary from 4 to 6 in the visible domain and reach up to 11 in the UV. As shown in Figure S3, the radiative damping of the scattering modes decreases especially in the higher order modes that lead to higher quality factor of large nDISC nanoantenna. Therefore, a significant amount of energy is exchanged between the fluorescent molecule and hybrid multipolar plasmons demonstrating nDISC's superior antenna performance in the visible.

However, to fully utilize the higher order modes for the fluorescence enhancement, we also need to analyze the quantum yield change or quenching effect of the emitters at the hotspot as mentioned earlier. In order to project the available LDOS of

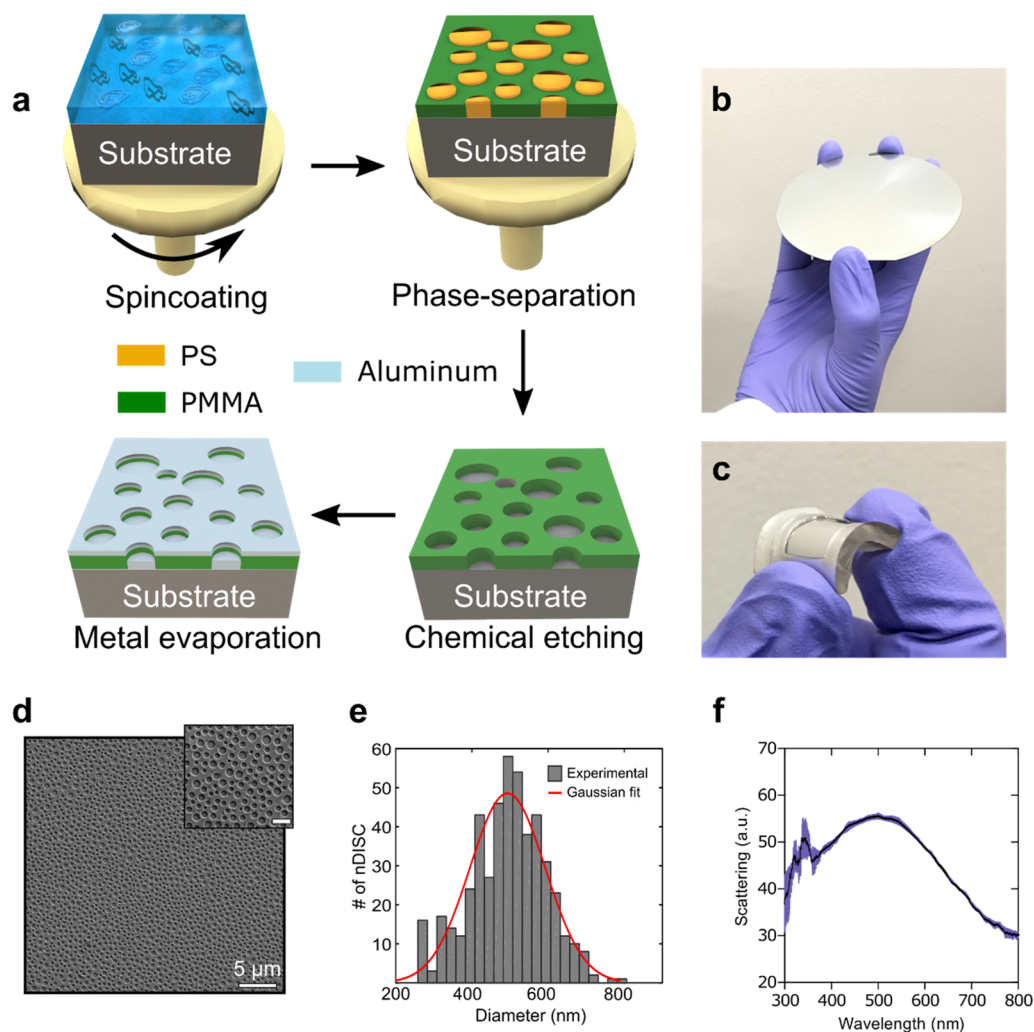


**Figure 3.** Fabrication of biomimetic Al nDISC nanoantenna metasurfaces. (a) The fabrication process for a biomimetic Al nDISC metasurface consists of three steps: The spin coating of the PMMA-PS mixture, the developing of the PS with cyclohexane, and the evaporation of the Al. Photographs of (b) 4 in. Si wafer and (c) flexible substrates with Al nDISC nanoantenna metasurfaces showing whitish appearance due to broadband scattering. (d) SEM image of the fabricated biomimetic metasurface projecting a dense distribution of nDISC nanoantennas. (e) Statistical analysis of the nDISC diameter fitted with a Gaussian profile with a mean diameter of 505 nm and a variance of 48 nm. (f) Dark-field scattering measurement of fabricated nDISC metasurfaces shows a broadband scattering behavior peaking at 505 nm.

nDISC antenna to an emitter, we calculated the relative enhancement factors (EF) of the radiative ( $\gamma_r$ ), nonradiative ( $\gamma_{nr}$ ), and total ( $\gamma_t$ ) emissions compared to those of the background and a lone nanodisk by placing a dipole emitter in the middle of the hotspot and at a point 2.5 nm from the hotspot center.<sup>26</sup> Figure 2c shows the broadband emission enhancement,  $\frac{\gamma_t}{\gamma_0}$  of nDISC over the visible spectrum. Such increase in emission or LDOS occurs from higher order plasmonic states within the circular hotspot (Figure 2d), providing additional pathways for emitted photons to couple and radiate into the far field and thereby increases the effective quantum yield of the emitter. The modified quantum yield,  $\eta$  of Cy3 due to nDISC antenna can be calculated as<sup>26,27</sup>

$$\eta = \frac{\frac{\gamma_r}{\gamma_0}}{(1 - \eta_0) + \frac{\gamma_r}{\gamma_0} + \frac{\gamma_{nr}}{\gamma_0}}$$

where  $\frac{\gamma_r}{\gamma_0} = 611.5$  and  $\frac{\gamma_{nr}}{\gamma_0} = 219.2$  are the radiative and nonradiative enhancements, respectively, of a nDISC-antenna-

coupled emitter at the emission wavelength of 568 nm. Therefore, nDISC antenna enhances the emission or quantum yield of Cy3 by a factor  $\frac{\eta}{\eta_0} = 7.28$ . Multiplying both the excitation and emission EFs yields a total theoretical fluorescence enhancement of 1056, which is in good agreement with measured experimental fluorescence enhancement shown in Figure 2f. Due to the out-of-plane excitation of the nDISC antenna irrespective of the in-plane light polarization at normal angle of incidence, vertically polarized fluorophore will provide the best theoretical enhancement. In practice, each molecule's dipole moment will be randomly oriented, resulting in the variation of experimental enhancement as shown in Figure 2f.

Typically, radiative components determine the overall emission enhancement, whereas photons that couple to nonradiative states undergo interband transitions and do not contribute to the emission process.<sup>26,27</sup> To single out the effects of radiative and nonradiative components, we have also plotted the contribution from the individual radiative and nonradiative components of nDISC in Figure S4 and compared with a lone Al nanodisk antenna. The radiative enhancements of nDISC are

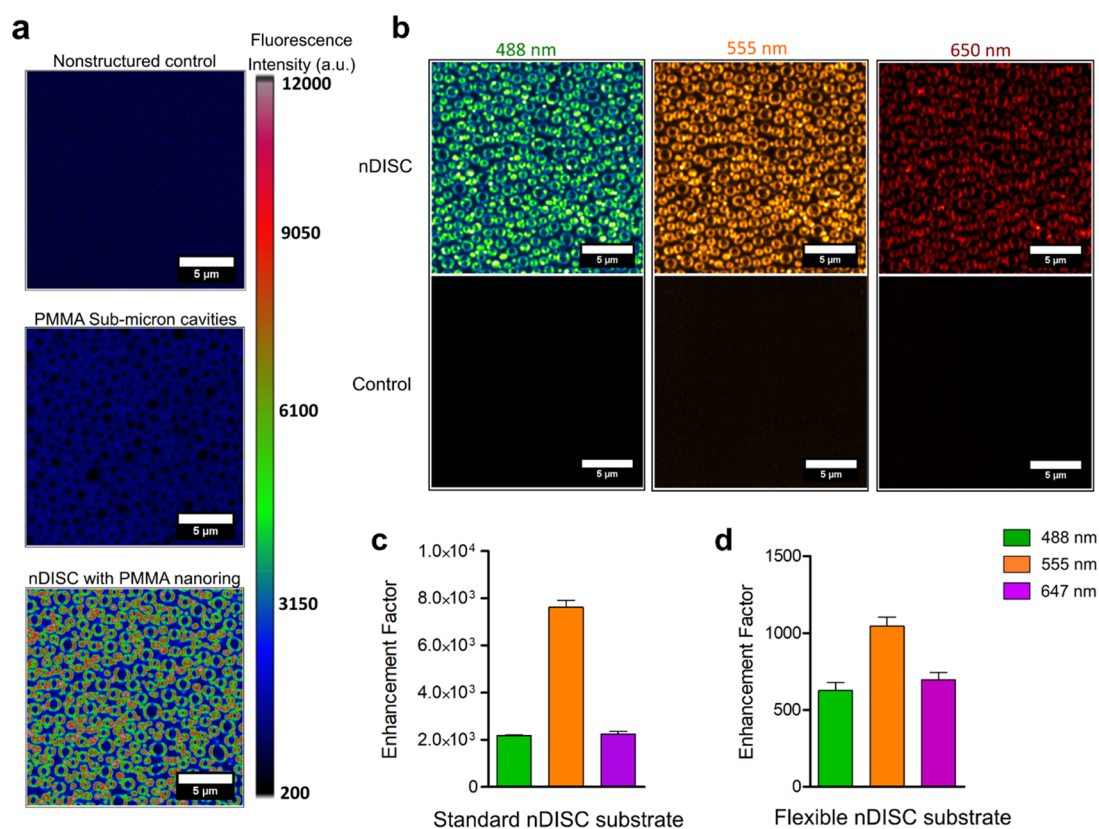


**Figure 4.** Broadband enhancement of fluorescence on Al nDISC nanoantenna. (a) Single-stranded DNA tagged with FAM was added on to substrates at the concentration of  $1 \mu\text{M}$  and imaged ( $\lambda_{\text{ex}} = 488 \text{ nm}$ ). PMMA submicron cavities showed higher fluorescence intensity due to enhanced capture of molecules as compared to the control. nDISC nanoantennas showed significant enhancement of signal over the control substrates. The color bar represents the fluorescence intensity values for all three substrates. (b) A mixture of fluorescently tagged aptamers diffusing in solution (concentration  $1 \mu\text{M}$ ) imaged under different channels ( $\lambda_{\text{ex}} = 488 \text{ nm}$  (FAM),  $555 \text{ nm}$  (Cy3), and  $647 \text{ nm}$  (Cy5) from left to right). Enhancement of fluorescence on Al metasurfaces as compared to nonstructured control is clearly visible. (c) Enhancement factor calculated for the three fluorophores with respect to a standard glass slide as control on metasurface wafers. For the substrates with PMMA nanoring, enhancement factors above 1000 were obtained for all three wavelengths. (d) Broadband fluorescence enhancement above 500 obtained on a flexible nDISC substrate fabricated using PDMS as the base material after 50 times bending. Scale bars are  $5 \mu\text{m}$  for all cases.

dominant in the visible spectrum, whereas a lone Al nanodisk antenna undergoes a large nonradiative enhancement that limits the antenna performance in the same spectral range. Quantitatively, radiative and nonradiative power components of an emitter experiences on average 6.5 and 1.8 times increase, respectively, if the optical antenna design is changed from a lone nanodisk to nDISC. Notably, a nDISC antenna offers higher radiative enhancement compared to nonradiative enhancement, supporting the positive role played by the strong radiative properties of the higher order modes on emission enhancement.

We utilized a biomimetic scalable fabrication technique to create large-scale nDISC metasurfaces either on a silicon (Si) wafer or a flexible substrate as illustrated in Figure 3a and demonstrated biosensing applications.<sup>30,31</sup> The details of the fabrication are included in the methods section. In brief, we spin-coated two phase-separated polymers, PMMA and polystyrene (PS), in a blend solution of butanone onto a 4 in. Si wafer that undergoes a three-dimensional phase separation in a humid environment and self-assembles into PS nanoislands in a PMMA matrix. We etched the PS islands with cyclohexane to form nanocavities in the PMMA matrix and directionally evaporated a thin aluminum layer on top of this substrate to form nDISC nanoantenna metasurfaces. Photographs of nDISC metasurfaces fabricated on a 4 in. wafer and flexible substrate are provided in Figure 3b,c. The substrate appears whitish, which stems from

the characteristic biomimetic broadband scattering due to the spatial distribution of long-range disordered nDISC antennas. We tailored the parameters of the fabrication process in such a manner that the average diameter of the nanocavities remains  $500 \text{ nm}$  (Figure 3d,e, see Materials and Methods section for details). The dark-field scattering measurement also confirms broadband properties of the substrate, as shown in Figure 3f. Such broadband properties are of particular interest for simultaneous diagnostics of numerous biomarkers labeled with different dyes on the same platform.

Fluorescence enhancement efficiency of the nDISC metasurfaces was tested using diffusing aptamers (concentration:  $1 \mu\text{M}$ ) and compared with various reference substrates (flat Al, PMMA cavities, microscopy glass slides). Images in Figure 4a show fluorescence signal obtained on nDISC metasurfaces as compared to flat Al surfaces and PMMA submicron cavities (fabricated on Si and with no Al coating). Our observations indicate that very weak fluorescence was obtained from flat aluminum surfaces (with native alumina on top). Substrates with PMMA submicron cavities (no metal) showed about 4-fold increase in fluorescence intensity as compared to these Al surfaces (Figure 4a) and 4- to 7-fold increase compared to standard glass slide (silica) surfaces (Figure S5). PMMA can act as an aggregator or local concentrator for biomolecules through increased propensity for physisorption, and it has been observed

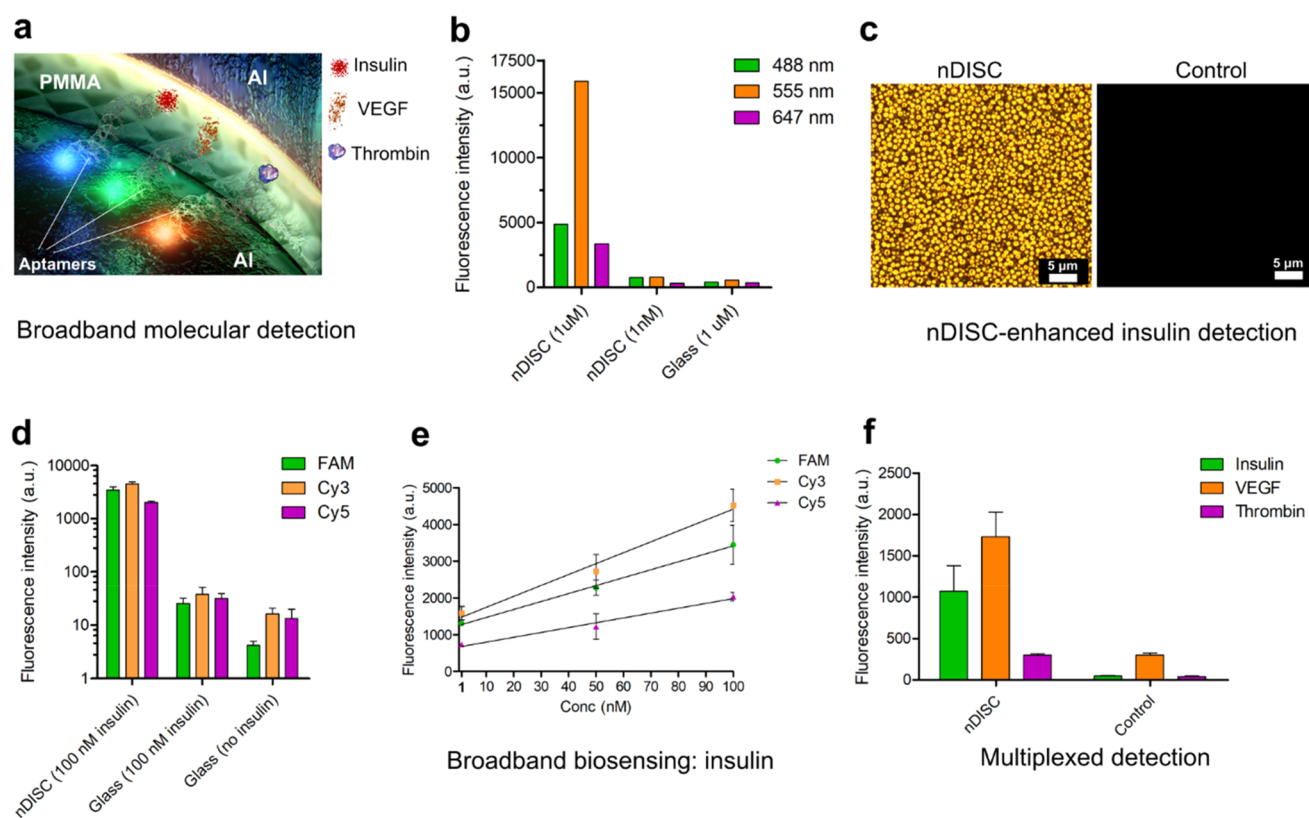


**Figure 5.** Broadband nDISC-enhanced multiplexed molecular detection. (a) Schematic showing the concept of broadband multiplexed molecular detection using Al nDISC metasurfaces. (b) Concentration-based enhancement analysis of signal from diffusing aptamers on nDISC vs control glass substrates. More than 1000-fold improvement in detection sensitivity is achieved as equivalent signals are obtained from a 1000-times diluted aptamer solution on the nDISC substrate as compared to control. (c) Detection of insulin adsorbed on the substrates using insulin-binding aptamers labeled with three fluorophores. Composite fluorescence image shows the difference in signal obtained from the nDISC surface compared to glass control. (d) Log-scale analysis of detection of 100 nM insulin on nDISC metasurfaces as compared to glass controls. (e) Detection of insulin over varying concentrations from 100 nM to 1 nM on a nDISC metasurface. (f) Detection of three biomarkers (insulin, VEGF, thrombin) on nDISC metasurfaces using three different aptamers tagged with FAM, Cy3, and Cy5 respectively. One fmol of each biomarker was added to the chips (conc, 100 pM; vol, 10  $\mu$ L). Fluorescence intensity is compared to a glass slide used as control.

in the past for both nucleic acids and proteins.<sup>32,33</sup> Previous reports have discussed nucleophilic interactions between amino or thiol-labeled DNA with PMMA<sup>32</sup> or hydrophobic interactions between nanotextured PMMA and proteins as the reason for elevated capture of these biomolecules.<sup>33</sup> While PMMA is frequently used as a resist during high-resolution lithography for fabrication of nanoplasmonic devices,<sup>34,35</sup> their potential for enhanced localized capture of molecules at the hotspot and resulting improved sensitivity have not been realized. We utilized PMMA as a dielectric nanoring sandwiched between two Al layers as part of nDISC metasurfaces and witnessed more than 10 $\times$  increase in raw fluorescence intensity over both flat Al surface (Figure 4a) as well as PMMA submicron cavities (Figures 4a and S6). These results indicate that the PMMA dielectric nanoring efficiently performs a dual role of facilitating highly localized electromagnetic enhancement as well as molecular concentration. Henceforth, we used PMMA as a dielectric medium in our nDISC metasurfaces.

As discussed earlier, our simulations indicate that the nDISC metasurfaces can enable significantly high near- and far-field enhancement in the visible regime which can lead to strong, broadband excitation and emission of fluorophores. This hypothesis was tested experimentally using DNA aptamers tagged with three different fluorophores (FAM, excitation: 488 nm, emission: 505 nm; Cy3, excitation: 555 nm, emission: 568

nm; and Cy5, excitation: 647 nm, emission: 670 nm), and their corresponding results are shown in Figure 4b. DNA tagged with these fluorophores was added on to the substrates together at a concentration of 1  $\mu$ M and imaged under a confocal microscope. Significant enhancement of fluorescence (>20-fold improvement for Cy3) from the substrates at all three emission wavelengths was observed. The EFs for these substrates compared to standard glass slides were calculated for these three wavelengths in the visible range. We obtained over 1000 times enhancement for all three cases, with effective enhancement for Cy3 close to 7500 (Figure 4c). The enhancement calculation for nDISC PMMA nanorings using glass slides as reference shows the effect of both optical and molecular concentration at the hotspot. We repeated the same experiment on a flexible nDISC substrate (fabricated on silicone elastomer instead of Si, details in methods section) after 50 times of bending and achieved above 500 times broadband enhancement as shown in Figure 4d. (The biosensing results discussed in the manuscript henceforth have been performed on the nonflexible Si wafer metasurface.) We also calculated the normalized enhancement (Figure S7), which eliminates the role of varying quantum efficiencies of the fluorophores and signifies the electromagnetic enhancement and enhanced molecular capture at the hotspots. These graphs indicate that while the Al nDISC metasurface still has the strongest electromagnetic confinement

in blue, it maintains strong performance for larger wavelengths, leading to highly effective broadband enhancement of fluorescence.

The highly efficient broadband fluorescence enhancement using the Al metasurfaces can be utilized for detection of low-concentration biomolecules on chip. The schematic (Figure 5a) shows the concept for broadband detection of different biomolecules. As an initial test, we analyzed concentration-varying signals from aptamers directly added to nDISC metasurfaces as compared to control glass samples (Figure 5b). Fluorescence intensity from molecules diluted 1000-fold (conc: 1 nM) onto the nDISC metasurfaces was equivalent to or higher than the signal obtained from molecules at the original concentration of 1  $\mu$ M on the glass control, for all three wavelengths. The results showed that more than a 1000-fold improvement in detection of the molecules over the visible wavelength regime can be obtained using these Al substrates.

Thereafter, the potential of the substrate for specific molecular detection was analyzed using insulin as a target molecule. When insulin-binding aptamers were tagged with three different fluorophores, insulin adsorbed on the nDISC metasurface was robustly and consistently detected at all three different wavelengths (center excitation wavelengths: 488, 555, and 647 nm) in the visible range (Figure 5c,d).<sup>36</sup> Detection of insulin is crucial for clinical diabetes treatment and management such as islet transplantation<sup>24</sup> or prevention of insulin overdose in diabetic patients.<sup>37</sup> We also obtained linear concentration-dependent sensing response with metasurface-enhanced fluorescence for insulin concentrations ranging from 1 nM to 100 nM (Figure 5e) consistently for all three wavelengths, suggesting that the metasurface can be capable of simultaneous detection of biomarkers at different wavelengths in the visible regime.

To demonstrate detection of multiple biomarkers at low concentrations for early on-chip disease diagnosis or more general multiplexed broadband biosensing, we chose to utilize insulin, VEGF, and thrombin as target molecules. VEGF is a regulator of angiogenesis and a crucial biomarker for several diseases including ocular vascular disease<sup>38</sup> and cancer with relevant plasma concentrations near 100 pM for tumors.<sup>25,39</sup> VEGF-binding aptamers have been used for both detection and management of associated ailments.<sup>25,38,40</sup> Thrombin is a serine protease which is used as a model biomarker for atherothrombosis (blood clotting), and aptamers have also been designed to specifically capture thrombin.<sup>41–43</sup> Free thrombin levels above 5 nM have been associated with a high risk of thrombosis.<sup>43</sup> These biomarkers were simultaneously added on the nDISC metasurfaces, each in the form of a 10  $\mu$ L droplet with molecular concentration 100 pM, that is, containing 1 fmol of each biomarker, followed by 1 h on-chip incubation. At these very low concentrations, the mean fluorescence signals from the nDISC samples were still significantly higher (about 6- to 10-fold increase in signal intensity) than the control substrates (Figure 5f).

## CONCLUSIONS

We have devised Al-based nDISC metasurfaces, which utilize hybrid multipolar plasmonic modes and generate 1000-fold broadband fluorescence enhancement of low quantum yield fluorophores. The fabrication method can be easily adapted for wafer-scale production, and nDISC can further be integrated in low-cost, soft, flexible, or microfluidic devices while retaining similar performance of fluorescence enhancement compared to nonflexible silicon-based nDISC substrates. Additionally,

nDISC antenna's efficient out-of-plane fluorescent beam redirection compared to conventional in-plane optical antenna can boost collection efficiency in a point-of-care platform for remote sensing (Figure S8). We further discussed the application of PMMA as a dielectric material within MIM gaps for simultaneous optical as well as localized molecular enhancement, leading to more than 1000-fold broadband enhancement in detection sensitivity. While PMMA remains a versatile and widely used material for nanofabrication, the direct application of nanoscale PMMA surfaces in nanophotonics devices as molecular aggregator has so far remained unexplored. There are several possibilities where the interaction of this material with molecules such as nucleic acids can be used for specific molecular detection as well as controlled molecular assembly for DNA origami. The optomolecular concentration capability of these substrates was then utilized for molecular detection in the full visible wavelength regime through multiplexed detection of three-different biomarkers for diabetes, ocular and cardiovascular diseases simultaneously. These results show that Al nDISC metasurfaces with PMMA nanorings can overcome traditional electromagnetic limitations suffered by Al-based plasmonic substrates,<sup>14</sup> overcoming more expensive Ag- and Au-based substrates (Figure S9) and are ideally suited for multiplexed bioanalysis for laboratory, clinical, and industrial applications.

## MATERIALS AND METHODS

**Fabrication of nDISC Nanoantenna and Metasurfaces.** First, 60 nm deep and 500 nm round cavities were milled by focused ion beam (FIB, FEI Nova 200 dual beam) on 50 nm-thick Au (deposited by Lesker Labline E-beam Evaporator, Kurt J. Lesker, rate 1  $\text{\AA}/\text{s}$ , pressure  $(3-5) \times 10^{-8}$  Torr) coated commercial single-side polished silicon wafers with thermally grown 1  $\mu\text{m}$   $\text{SiO}_2$  (University Wafers, Boston, USA). The remaining Au coating was lifted-off using a commercial gold-etchant followed by directional 50 nm Al evaporation (Lesker Labline E-beam Evaporator, Kurt J. Lesker, rate 1  $\text{\AA}/\text{s}$ , pressure  $(3-5) \times 10^{-8}$  Torr) on the  $\text{SiO}_2$  cavities to form the final nDISC nanoantennas as shown in Figure 1.

To fabricate large-scale nDISC nanoantenna metasurfaces, commercial single-side polished Si wafers (University Wafers, Boston, USA) were sequentially cleaned with acetone, isopropanol (IPA), and distilled water. Then, either wafers or spin-coated PDMS films (Sylgard 184 elastomer base mixed with curing agent in a ratio of 15:1) were dried with  $\text{N}_2$  followed with 60 s of  $\text{O}_2$  plasma. Poly(methyl methacrylate) (PMMA,  $M_w = 9.59$  kg/mol, Polymer Standards Service GmbH, Germany) and polystyrene (PS,  $M_w = 96$  kg/mol, Polymer Standards Service GmbH, Germany) were dissolved in methyl ethyl ketone (MEK, Sigma-Aldrich Co. LLC, USA) at mass ratios of 6:4 with a concentration of 20 mg/mL. The solution was spin coated onto the substrates at a speed of 3500 rpm for 30 s with relative humidity of 45%. The samples were then rinsed twice in cyclohexane for 60 s and dried in a stream of  $\text{N}_2$  to remove the PS islands, and the PMMA thickness ( $x$  nm) was measured with atomic force microscopy (AFM). Afterward, Al of  $x-10$  nm was evaporated at ultrahigh vacuum (Lesker Labline E-beam Evaporator, Kurt J. Lesker, rate 1  $\text{\AA}/\text{s}$ , pressure  $(3-5) \times 10^{-8}$  Torr) on the PMMA cavities to form the final nDISC nanoantenna metasurfaces (Figure 3). The measured gap of nDISC metasurfaces is  $5.28 \pm 1.19$  nm ( $n = 50$ ).

**Surface Analysis.** The surface patterns were examined using scanning electron microscopy (FEI Nova 200 NanoLab Dualbeam) and AFM (Dimension Icon, Bruker Corporation, USA) for extracting the diameter distribution and measuring the depth of the cavities, respectively. ImageJ (<http://imagej.nih.gov/ij/>) was used to perform a statistical analysis of different morphological parameters of fabricated samples.

**Optical Analysis.** A customized optical microscope operating in dark-field mode was used for the microspectroscopic investigation of

the fabricated nDISC nanoantenna and metasurfaces in water. A halogen lamp was used as a light source using a 100× objective with a numerical aperture of NA = 0.95. The scattered light was collected in a confocal configuration and analyzed using a spectrometer (AvaSpec-ULS2048x64-USB2). A 50 μm and 400 μm core optical fiber was used to get a spatial resolution of 1 μm and 20 μm to characterize the scattering of single FIB-milled nDISC and biomimetic metasurfaces, respectively.

**FDTD Simulations.** 3D optical simulations of nDISC nanoantenna and lone nanodisk for calculating and comparing the field intensity and quantum yield enhancements were set up in the FDTD Maxwellian solver Lumerical. 3 nm of native alumina is considered on top of Al nanostructures for all simulations. Scattering and absorption cross-section spectra were calculated using TFSF plane wave illumination at normal incidence. LDOS studies to calculate radiative, nonradiative, and quantum yield enhancements of a dipole due to nDISC nanoantenna were performed using Green's function analysis in Lumerical.

**Aptamer Assays.** Single-stranded DNA or aptamers were custom ordered from Integrated DNA Technologies, USA. The aptamers were fluorescently labeled at the 5' end, and a spacer sequence was placed between the dye and rest of the DNA sequence to allow proper folding. For broadband insulin detection tests (Figure 5c–e), three batches of insulin-binding aptamers were ordered with different fluorophores attached at the 5' end. Insulin-binding aptamer (IBA): 5'-Dye-/A/iSP9/-GGTGGTGGGGGGGGTTGGTAGGG TGTCTT C-3', where Dye = FAM (fluorescein), Cy3, or Cy5.

For multiplexed detection of three biomarkers IBA tagged with FAM was used. VEGF and thrombin-binding aptamers were separately ordered as follows: VEGF-binding aptamer (VEGF-BA): 5'-Cy3-/A/iSp9/-TGTGGGGGTGGACGGGC CGG GTA GA-3'. Thrombin-binding aptamer (TBA): 5'-Cy5-/A/iSP9/-AGTCCGTGGTAGGG-CAGGTTG GGGTGAC T-3'

These aptamers were obtained lyophilized and stored in Tris-EDTA (TE) buffer (10 mM Tris-HCl, 1 mM EDTA, pH 7.4) at −20 °C at a concentration of 100 μM. For experiments concerning fluorescence intensity comparison, aptamers labeled with three fluorophores were diluted in Tris-HCl buffer (pH 7.4) and mixed together at a concentration of 1 μM. Thereafter, a drop (30 μL) of the mixture was added onto the substrates. A coverslip was placed over the droplets, and samples were imaged.

Insulin, VEGF, and thrombin were obtained from Sigma-Aldrich, USA. Stock solutions with molecular concentration 1 μM were prepared in PBS buffer (pH 7.4) and stored at −20 °C. Thrombin solution included 0.1% (w/v) BSA for stability. Prior to use, the samples were diluted to desired concentrations, and 10 μL of each sample was added to the substrates. The samples were placed in a humidity chamber and left undisturbed for an hour. The samples were then washed with PBS for 30 min. A droplet of BSA (1%) (30 μL) was added to the samples to account for any noncoated regions on the substrates and left undisturbed (in a humidity chamber) for an hour. The samples were washed again with PBS buffer. Stock aptamer solutions were diluted in a Tris-HCl DNA folding buffer (10 mM Tris-HCl, 137 mM sodium chloride, 8 mM sodium phosphate dibasic, 2 mM potassium phosphate monobasic, and 1 mM MgCl<sub>2</sub>, pH 7.4), heated to 95 °C, and allowed to cool down to room temperature for 30 min. The aptamers were then added to the samples at a concentration of 1 μM and allowed to bind for 1 h. The samples were washed with the same folding buffer thereafter. A coverslip was placed over the samples for imaging. The sample was never allowed to dry during these steps to avoid any drying-based concentration artifacts. Addition of molecules postwashing was performed while maintaining a thin film of buffer solution on the chips.

**Fluorescence Imaging.** Fluorescence images were obtained using an inverted Zeiss confocal laser scanning microscope (LSM 800) at the Beckman Imaging Center at California Institute of Technology. Time-lapse and variable laser power fluorescence analyses with the setup for different dye-tagged aptamers are shown in Figures S10 and S11 to support the chosen parameters (imaging time, laser power) for the experiments. The samples were placed under a 100×, oil immersion

objective (NA: 1.46), and excitation laser wavelengths 488, 555, and 650 nm were used for the appropriate fluorophores.

**Image Analysis.** Images were analyzed using Zen software from Carl Zeiss and open-source software FIJI (ImageJ).<sup>44</sup> For computing the mean fluorescence from the hotspots, a circular area was drawn encompassing the hotspots, and the fluorescence values were analyzed. Background intensity with no added fluorophores was collected for all substrates and subtracted during fluorescence intensity analysis. Graphs were created in Matlab\_R2019a and Graphpad Prism 5.01.

## ASSOCIATED CONTENT

### Supporting Information

The Supporting Information is available free of charge on the ACS Publications website at DOI: 10.1021/acsnano.9b02926.

Detailed enhancement factor calculations, additional simulated data of single nanodisk and nDISC, scattering and absorption cross-section spectra and LDOS studies to calculate radiative, nonradiative, and quantum yield enhancements, additional supporting experimental scattering and fluorescence data with flexible substrate and other noble materials. All the research data supporting the publication are included (PDF)

## AUTHOR INFORMATION

### Corresponding Author

\*E-mail: [hyuck.choo@samsung.com](mailto:hyuck.choo@samsung.com); [hchoo@caltech.edu](mailto:hchoo@caltech.edu).

### ORCID

Radwanul Hasan Siddique: 0000-0001-7494-5857

Shailabh Kumar: 0000-0001-5383-3282

### Author Contributions

These authors contributed equally to this work. R.H.S. and S.K. conceived the idea and equally contributed in the study. R.H.S. and S.K. designed the analyses, performed the experiments. H.C. provided supervision to R.H.S. and S.K. H.K. and V.N. assisted in the simulation process. R.H.S., S.K., and H.C. wrote the manuscript. All authors discussed the results and commented on the manuscript.

### Notes

The authors declare no competing financial interest.

## ACKNOWLEDGMENTS

We gratefully acknowledge critical support and infrastructure provided for this work by the Kavli Nanoscience Institute at Caltech. We thank Haeri Park for fruitful discussion on the manuscript. Imaging was performed in the Biological Imaging Facility, with the support of the Caltech Beckman Institute and the Arnold and Mabel Beckman Foundation. The research was funded by a Samsung Global Research Outreach program.

## REFERENCES

- (1) Eid, J.; Fehr, A.; Gray, J.; Luong, K.; Lyle, J.; Otto, G.; Peluso, P.; Rank, D.; Baybayan, P.; Bettman, B.; et al. Real-Time DNA Sequencing From Single Polymerase Molecules. *Science* **2009**, *323*, 133–138.
- (2) Flusberg, B. A.; Webster, D. R.; Lee, J. H.; Travers, K. J.; Olivares, E. C.; Clark, T. A.; Korlach, J.; Turner, S. W. Direct Detection of DNA Methylation During Single-Molecule, Real-Time Sequencing. *Nat. Methods* **2010**, *7*, 461–465.
- (3) Ambrosi, A.; Airo, F.; Merkoci, A. Enhanced Gold Nanoparticle Based ELISA for a Breast Cancer Biomarker. *Anal. Chem.* **2010**, *82*, 1151–1156.
- (4) Chen, S.; Svedendahl, M.; Van Duyne, R. P.; Käll, M. Plasmon-Enhanced Colorimetric ELISA With Single Molecule Sensitivity. *Nano Lett.* **2011**, *11*, 1826–1830.

- (5) De La Rica, R.; Stevens, M. M. Plasmonic ELISA for the Ultrasensitive Detection of Disease Biomarkers With the Naked Eye. *Nat. Nanotechnol.* **2012**, *7*, 821–824.
- (6) Acuna, G.; Möller, F.; Holzmeister, P.; Beater, S.; Lalkens, B.; Tinnefeld, P. Fluorescence Enhancement at Docking Sites of DNA-Directed Self-Assembled Nanoantennas. *Science* **2012**, *338*, 506–510.
- (7) Kinkhabwala, A.; Yu, Z.; Fan, S.; Avlasevich, Y.; Müllen, K.; Moerner, W. Large Single-Molecule Fluorescence Enhancements Produced by a Bowtie Nanoantenna. *Nat. Photonics* **2009**, *3*, 654–657.
- (8) Punj, D.; Mivelle, M.; Moparthy, S. B.; Van Zanten, T. S.; Rigneault, H.; Van Hulst, N. F.; García-Parajó, M. F.; Wenger, J. A Plasmonic/Antenna-in-Box/Platform for Enhanced Single-Molecule Analysis at Micromolar Concentrations. *Nat. Nanotechnol.* **2013**, *8*, 512–516.
- (9) Boltasseva, A.; Atwater, H. A. Low-Loss Plasmonic Metamaterials. *Science* **2011**, *331*, 290–291.
- (10) Knight, M. W.; Liu, L.; Wang, Y.; Brown, L.; Mukherjee, S.; King, N. S.; Everitt, H. O.; Nordlander, P.; Halas, N. J. Aluminum Plasmonic Nanoantennas. *Nano Lett.* **2012**, *12*, 6000–6004.
- (11) Naik, G. V.; Schroeder, J. L.; Ni, X.; Kildishev, A. V.; Sands, T. D.; Boltasseva, A. Titanium Nitride as a Plasmonic Material for Visible and Near-Infrared Wavelengths. *Opt. Mater. Express* **2012**, *2*, 478–489.
- (12) Knight, M. W.; King, N. S.; Liu, L.; Everitt, H. O.; Nordlander, P.; Halas, N. J. Aluminum for Plasmonics. *ACS Nano* **2014**, *8*, 834–840.
- (13) Olson, J.; Manjavacas, A.; Liu, L.; Chang, W.-S.; Foerster, B.; King, N. S.; Knight, M. W.; Nordlander, P.; Halas, N. J.; Link, S. Vivid, Full-Color Aluminum Plasmonic Pixels. *Proc. Natl. Acad. Sci. U. S. A.* **2014**, *111*, 14348–14353.
- (14) Gérard, D.; Gray, S. K. Aluminium Plasmonics. *J. Phys. D: Appl. Phys.* **2015**, *48*, 184001.
- (15) Martin, J.; Kociak, M.; Mahfoud, Z.; Proust, J.; Gérard, D.; Plain, J. High-Resolution Imaging and Spectroscopy of Multipolar Plasmonic Resonances in Aluminum Nanoantennas. *Nano Lett.* **2014**, *14*, 5517–5523.
- (16) Sharma, B.; Cardinal, M. F.; Ross, M. B.; Zrimsek, A. B.; Bykov, S. V.; Punihale, D.; Asher, S. A.; Schatz, G. C.; Van Duyne, R. P. Aluminum Film-Over-Nanosphere Substrates for Deep-UV Surface-Enhanced Resonance Raman Spectroscopy. *Nano Lett.* **2016**, *16*, 7968–7973.
- (17) Tian, S.; Neumann, O.; McClain, M. J.; Yang, X.; Zhou, L.; Zhang, C.; Nordlander, P.; Halas, N. J. Aluminum Nanocrystals: A Sustainable Substrate for Quantitative SERS-Based DNA Detection. *Nano Lett.* **2017**, *17*, 5071–5077.
- (18) Wiecha, P. R.; Mennemanteuil, M.-M.; Khlopin, D.; Martin, J.; Arbouet, A.; Gérard, D.; Bouhelier, A.; Plain, J.; Cuche, A. Local Field Enhancement and Thermoplasmonics in Multimodal Aluminum Structures. *Phys. Rev. B: Condens. Matter Mater. Phys.* **2017**, *96*, 035440.
- (19) Giannini, V.; Fernández-Domínguez, A. I.; Sonnefraud, Y.; Roschuk, T.; Fernández-García, R.; Maier, S. A. Controlling Light Localization and Light–Matter Interactions With Nanoplasmonics. *Small* **2010**, *6*, 2498–2507.
- (20) Chikkaraddy, R.; de Nijs, B.; Benz, F.; Barrow, S. J.; Scherman, O. A.; Rosta, E.; Demetriadou, A.; Fox, P.; Hess, O.; Baumberg, J. J. Single-Molecule Strong Coupling at Room Temperature in Plasmonic Nanocavities. *Nature* **2016**, *535*, 127–130.
- (21) Kongsuwan, N.; Demetriadou, A.; Chikkaraddy, R.; Benz, F.; Turek, V. A.; Keyser, U. F.; Baumberg, J. J.; Hess, O. Suppressed Quenching and Strong-Coupling of Purcell-Enhanced Single-Molecule Emission in Plasmonic Nanocavities. *ACS Photonics* **2018**, *5*, 186–191.
- (22) Chikkaraddy, R.; Zheng, X.; Benz, F.; Brooks, L. J.; de Nijs, B.; Carnegie, C.; Kleemann, M.-E.; Mertens, J.; Bowman, R. W.; Vandenbosch, G. A.; et al. How Ultranarrow Gap Symmetries Control Plasmonic Nanocavity Modes: From Cubes to Spheres in the Nanoparticle-on-Mirror. *ACS Photonics* **2017**, *4*, 469–475.
- (23) Siddique, R. H.; Mertens, J.; Hölscher, H.; Vignolini, S. Scalable and Controlled Self-Assembly of Aluminum-Based Random Plasmonic Metasurfaces. *Light: Sci. Appl.* **2017**, *6*, No. e17015.
- (24) Cho, H.; Kumar, S.; Yang, D.; Vaidyanathan, S.; Woo, K.; Garcia, I.; Shue, H. J.; Yoon, Y.; Ferreri, K.; Choo, H. Surface-Enhanced Raman Spectroscopy-Based Label-Free Insulin Detection at Physiological Concentrations for Analysis of Islet Performance. *ACS Sens* **2018**, *3*, 65–71.
- (25) Lee, H.-S.; Kim, K. S.; Kim, C.-J.; Hahn, S. K.; Jo, M.-H. Electrical Detection of VEGFs for Cancer Diagnoses Using Anti-Vascular Endothelial Growth Factor Aptamer-Modified Si Nanowire FETs. *Biosens. Bioelectron.* **2009**, *24*, 1801–1805.
- (26) Novotny, L.; Hecht, B. *Principles of Nano-Optics*; Cambridge University Press: Cambridge, 2012.
- (27) Mack, D. L.; Cortés, E.; Giannini, V.; Török, P.; Roschuk, T.; Maier, S. A. Decoupling Absorption and Emission Processes in Super-Resolution Localization of Emitters in a Plasmonic Hotspot. *Nat. Commun.* **2017**, *8*, 14513.
- (28) Eizner, E.; Avayu, O.; Ditscovski, R.; Ellenbogen, T. Aluminum Nanoantenna Complexes for Strong Coupling Between Excitons and Localized Surface Plasmons. *Nano Lett.* **2015**, *15*, 6215–6221.
- (29) Langhammer, C.; Schwind, M.; Kasemo, B.; Zoric, I. Localized Surface Plasmon Resonances in Aluminum Nanodisks. *Nano Lett.* **2008**, *8*, 1461–1471.
- (30) Narasimhan, V.; Siddique, R. H.; Lee, J. O.; Kumar, S.; Ndjamen, B.; Du, J.; Hong, N.; Sretavan, D.; Choo, H. Multifunctional Biophotonic Nanostructures Inspired by the Longtail Glasswing Butterfly for Medical Devices. *Nat. Nanotechnol.* **2018**, *13*, 512–519.
- (31) Siddique, R. H.; Donie, Y. J.; Gomard, G.; Yalamanchili, S.; Merdzhanova, T.; Lemmer, U.; Hölscher, H. Bioinspired Phase-Separated Disordered Nanostructures for Thin Photovoltaic Absorbers. *Sci. Adv.* **2017**, *3*, No. e1700232.
- (32) Fixe, F.; Dufva, M.; Telleman, P.; Christensen, C. B. V. One-Step Immobilization of Aminated and Thiolated DNA Onto Poly (methylmethacrylate)(PMMA) Substrates. *Lab Chip* **2004**, *4*, 191–195.
- (33) Tsougeni, K.; Tserepi, A.; Constantoudis, V.; Gogolides, E.; Petrou, P.; Kakabakos, S. Plasma Nanotextured PMMA Surfaces for Protein Arrays: Increased Protein Binding and Enhanced Detection Sensitivity. *Langmuir* **2010**, *26*, 13883–13891.
- (34) Broers, A. N. Resolution Limits of PMMA Resist for Exposure With 50 kV Electrons. *J. Electrochem. Soc.* **1981**, *128*, 166–170.
- (35) Chou, S. Y.; Krauss, P. R.; Renstrom, P. J. Imprint Lithography With 25-Nanometer Resolution. *Science* **1996**, *272*, 85–87.
- (36) Yoshida, W.; Mochizuki, E.; Takase, M.; Hasegawa, H.; Morita, Y.; Yamazaki, H.; Sode, K.; Ikebukuro, K. Selection of DNA Aptamers Against Insulin and Construction of an Aptameric Enzyme Subunit for Insulin Sensing. *Biosens. Bioelectron.* **2009**, *24*, 1116–1120.
- (37) Mork, T. A.; Killeen, C. T.; Patel, N. K.; Dohnal, J. M.; Karydes, H. C.; Leikin, J. B. Massive Insulin Overdose Managed by Monitoring Daily Insulin Levels. *Am. J. Ther* **2011**, *18*, e162–e166.
- (38) Ng, E. W.; Shima, D. T.; Calias, P.; Cunningham, E. T., Jr; Guyer, D. R.; Adams, A. P. Pegaptanib, a Targeted Anti-VEGF Aptamer for Ocular Vascular Disease. *Nat. Rev. Drug Discovery* **2006**, *5*, 123–132.
- (39) Stefanini, M. O.; Wu, F. T.; Mac Gabhann, F.; Popel, A. S. Increase of Plasma VEGF After Intravenous Administration of Bevacizumab Is Predicted by a Pharmacokinetic Model. *Cancer Res.* **2010**, *70*, 9886–9894.
- (40) Nonaka, Y.; Sode, K.; Ikebukuro, K. Screening and Improvement of an Anti-VEGF DNA Aptamer. *Molecules* **2010**, *15*, 215–225.
- (41) Luo, X.; Davis, J. J. Electrical Biosensors and the Label Free Detection of Protein Disease Biomarkers. *Chem. Soc. Rev.* **2013**, *42*, 5944–5962.
- (42) Tasset, D. M.; Kubik, M. F.; Steiner, W. Oligonucleotide Inhibitors of Human Thrombin That Bind Distinct Epitopes. *J. Mol. Biol.* **1997**, *272*, 688–698.
- (43) Trapaidze, A.; Héroult, J.-P.; Herbert, J.-M.; Bancaud, A.; Gué, A.-M. Investigation of the Selectivity of Thrombin-Binding Aptamers for Thrombin Titration in Murine Plasma. *Biosens. Bioelectron.* **2016**, *78*, 58–66.
- (44) Schindelin, J.; Arganda-Carreras, I.; Frise, E.; Kaynig, V.; Longair, M.; Pietzsch, T.; Preibisch, S.; Rueden, C.; Saalfeld, S.; Schmid, B.; et al. Fiji: An Open-Source Platform for Biological-Image Analysis. *Nat. Methods* **2012**, *9*, 676–682.